ADVANCED MATERIALS INTERFACES
Open Access
www.advmatinterfaces.de

Multifunctional Ultrathin Recycled PET-Based Membrane for Electromagnetic Interference Shielding, Antibacterial and Thermal Management

Zhuomin Jiang, Shuqing Piao, Taewook Park, Shengjun Li, Yonghwan Kim, Eunji Lee, Chaewon Bae, Yejin Lee, Hyung-Jun Im, Jungsuek Oh, Yuanzhe Piao, and Kangwon Lee**

With the advent of 5G and the Internet of Things (IoT), there is a high demand for lightweight and flexible electromagnetic interference (EMI) shielding membranes with multifunctional capabilities. However, the rapid advancement of technology has led to environmental deterioration, emphasizing the significance of eco-friendly and sustainable materials for EMI shielding. In this study, a novel environment-friendly EMI shielding membrane with electric thermotherapy function and antibacterial properties is developed. The membrane substrate utilizes recycled polyethylene terephthalate (rPET) and is sequentially coated with synthesized FeCo@C nanoparticles (NPs) and silver nanowires (Ag NWs). The membrane is then dip-coated with PDMS to modify the surface superhydrophobicity. Experimental results affirm that the developed environment-friendly EMI shielding membrane possesses exceptional shielding efficiency (68 dB) and can be effectively utilized for safe and low-voltage thermotherapy (137 °C by 2 V) while exhibiting antibacterial properties.

1. Introduction

The explosion of the internet brings a phenomenal development of electronic devices. With the rapid development of wireless communication, network generation is marching toward 5G. Simultaneously, the aerospace sector has witnessed remarkable progress in space exploration. However, these advancements in 5G technology and space exploration have also resulted in a growing concern regarding electromagnetic interference (EMI) and its detrimental effects on electronic devices, environmental surroundings, and human health.[1–3] Such concerns have a substantial impact on industries such as electronics, automotive, and aerospace.[4,5] EMI shielding refers to creating barriers or enclosures to prevent the transmission of electromagnetic radiation, which can be achieved through various mechanisms, including reflection resulting from the interaction between the electromagnetic field and the surface free charge carriers of highly conductive materials.[6,7] EMI can also be absorbed when the electromagnetic field interacts with electric or magnetic dipoles of magnetic materials. In addition, internal reflection occurring within the structure of the shielding materials

Z. Jiang, S. Piao, Y. Kim, E. Lee, Y. Lee, H.-J. Im, Y. Piao, K. Lee
Department of Applied Bioengineering, Graduate School of Convergence Science and Technology
Seoul National University
Seoul 08826, Republic of Korea
E-mail: parkat9@snu.ac.kr; kangwonlee@snu.ac.kr

T. Park, J. Oh
Department of Electrical and Computer Engineering
Seoul National University
Gwanak-ro, Gwanak-gu, Seoul 08826, Republic of Korea

S. Li, H.-J. Im
Department of Molecular Medicine and Biopharmaceutical Sciences, Graduate School of Convergence Science and Technology
Seoul National University
Seoul, Republic of Korea

C. Bae
Program in Nanoscience and Technology, Graduate School of Convergence Science and Technology
Seoul National University
Seoul 08826, Republic of Korea

H.-J. Im
Cancer Research Institute
Seoul National University
Seoul 03080, Republic of Korea

H.-J. Im, K. Lee
Research Institute for Convergence Science
Seoul National University
Suwon-si, Gyeonggi-do 08826, Republic of Korea

Y. Piao
Advanced Institutes of Convergence Technology
Suwon-si, Gyeonggi-do 16229, Republic of Korea

The ORCID identification number(s) for the author(s) of this article can be found under https://doi.org/10.1002/admi.202301047

DOI: 10.1002/admi.202301047

also contributes to their effectiveness. The upgraded EMI shielding materials focus on lightweight and flexible recycled polymer-based membranes, incorporating nano-sized inorganic fillers to achieve high EMI shielding efficiency.[8,9] It has remarkable potential for minimizing aerospace and automotive products and bendable shielding coverage, such as compact devices and wearable electronics.[10]

However, in today's technology-driven world, the imperative of environmentally friendly EMI shielding that can preserve resources and foster sustainable technological advancement has been emphasized. As an example, Recycled materials have emerged in EMI shielding to protect the environment and save resources, including cigarette filters, carbon fibers, leather solid waste, and polyethylene terephthalate (PET).[11–17] Especially, PET has been applied to various areas (bottles, textiles, electronics) with excellent tensile strength, thermal stability, clarity, and chemical resistance.[18] Nonetheless, the growing consumption of non-degradable PET raises concerns about environmental pollution and recycling.[19] For this reason, efficient PET recycling methods have gained attention as an alternative to expensive and complex biodegradation. These methods can be categorized into chemical and mechanical approaches. Chemical recycling methods, such as hydrolysis, alcoholysis, and aminolysis may lead to unintended secondary pollution.[13] On the other hand, mechanical recycling methods involve upcycling PET waste into diverse structures, such as concrete, non-woven fabric, and yarns.[20–28] Thus, in light of growing concerns about the environmental impact of non-degradable PET materials and the desire to foster sustainable technological advancement, mechanical recycling methods can be a promising solution for eco-friendly EMI shielding.

Moreover, to create a lightweight and high-performance eco-friendly EMI shielding membrane, the choice of inorganic material fillers that can be incorporated with dielectric PET polymer is crucial. These fillers contribute to the membrane's EMI shielding capabilities while providing additional functions such as electrical conductivity and heat generation.[29–31] The EMI waves can be absorbed by magnetic materials such as iron (Fe), cobalt (Co), and nickel (Ni).[32] FeCo stands out among these materials due to its high Curie temperature, magneto-crystalline anisotropy, and saturation magnetization, making it a promising candidate for microwave absorption applications.[33] Nevertheless, the susceptibility to oxidation hinders the practical application of FeCo nanoparticles (NPs). To mitigate this issue, a carbon shell layer is a lightweight candidate that can help protect FeCo NPs from oxidation while enhancing microwave absorption and reflection.[34] The FeCo@C core–shell structure has attracted considerable attention for its potential in practical EMI shielding applications. Another alternative within the category of inorganic materials is the utilization of some highly conductive metals such as copper (Cu), silver (Ag), gold (Au), and platinum (Pt).[35,36] These metals serve the EMI shielding by reflecting EMI waves instead of absorbing them. Among these materials, silver nanowires (Ag NWs) exhibit an outstanding electrically conductive network for shielding EMI.[37] It possesses high conductivity and low sheet resistance that can generate heat with a safe voltage for thermotherapy applications.[38] Furthermore, they exhibit antibacterial properties, adding to their versatility and usefulness.

Herein, we have developed a novel multifunctional EMI shielding membrane using a recycled polyethylene terephthalate (rPET) electrospun membrane. The membrane was coated with synthesized FeCo@C NPs and Ag NWs through a process involving sonication and dip-coating. To stabilize the coating particles and impart superhydrophobicity to the membrane surface, polydimethylsiloxane (PDMS) was dispersed in hexane and dip-coated onto the membrane surface (**Figure 1**). The resulting rPET/FeCo@C/Ag90/PDMS20 membrane exhibited a shielding efficiency of 68 dB in the X band despite having a conductive thickness of only 12.33 μm. The high electrical conductivity of the incorporated Ag NWs allows for the potential application of safe heat therapy, as the therapy can be conducted at voltages below 1 V. Specifically, a temperature of 40.3 °C, which is considered safe for the human body, can be reached by operating the heat therapy at 0.8 V. Additionally, the superhydrophobic surface achieved through PDMS dip-coating enhances the antibacterial properties of the rPET/FeCo@C/Ag90 membrane. Consequently, this environmentally friendly and versatile multifunctional EMI shielding membrane can find applications in various fields, such as deicing, energy generation, and antibacterial treatments.

2. Results and Discussion

2.1. Fabrication of rPET/FeCo@C NPs/Ag NWs/PDMS Membrane

The membrane substrate is fabricated through electrospinning, utilizing dissolved PET bottle-cutting pieces in a blended solution of chloroform, trifluoroacetic acid, and dichloromethane. From **Figure 2**a,b, the electrospun rPET fiber has a mean diameter of 1.33 ± 0.69 μm. FeCo@C core–shell NPs are synthesized by pyrolyzing the FeCo Prussian blue analogs (PBAs) nanocube, and the FeCo PBA nanocube was prepared by a chemical precipitation method. The average diameter of FeCo@C NPs is 76.5 ± 17.48 nm (Figure 2a,b). Ag NWs are synthesized through the polyol method, resulting in an average length of 11.77 ± 3.66 μm with ≈51.54 nm of diameter. Figure 2c,d shows the membrane surface changes by a sequential coating of FeCo@C NPs and Ag NWs. FeCo@C NPs indirect sonication coating changes the electrospun rPET membrane surface into black, and the SEM image presents that FeCo@C NPs are assembled on the rPET fiber surface. The assistance of sonication can help the dispersion of FeCo@C NPs in the ethanol and intensively drive them to hit the electrospun fibers for embedding uniformly to the membrane surface.[39]

It shows that the membrane surface changed from black into silver after the Ag NWs dip-coating procedure, and the SEM result (Figure 2c,d) shows that Ag NWs were perfectly covered on the membrane surface. The Ag NWs colloids were driven toward the membrane by the capillary force, due to the air–liquid–solid triple-phase line of the meniscus. The capillary force results in the adhesion of Ag NWs on the rPET/FeCo@C membrane surface.[40–42] Figure 2e demonstrates the existence of rPET, FeCo@C, Ag NWs, and PDMS by EDS mapping. The stability of the binding between conductive particles and rPET fibers was investigated under ethanol exposure and rotation for 1, 3, and 9 h, as illustrated in Figure S1 (Supporting Information).

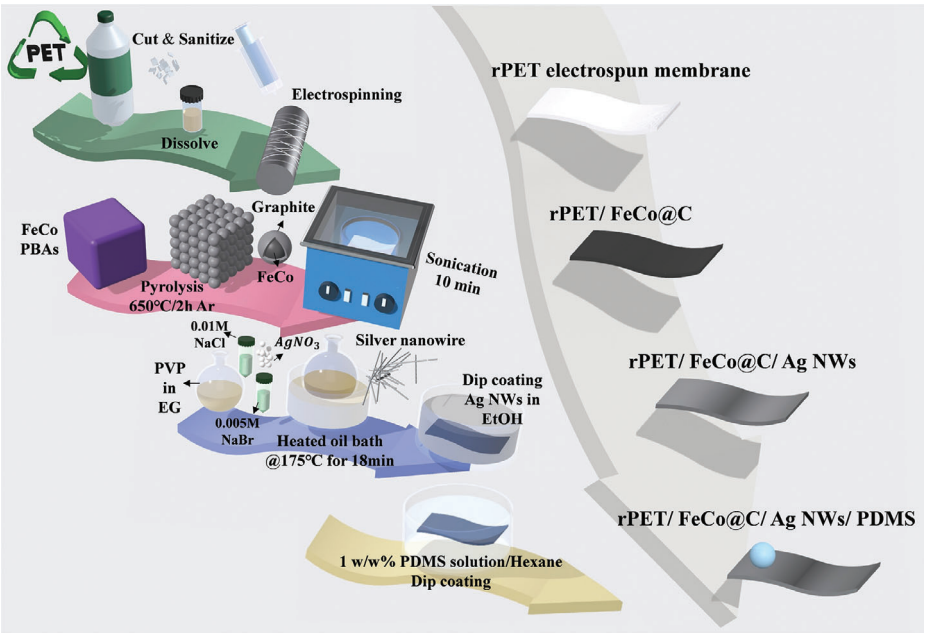

Figure 1. The scheme illustration of rPET/FeCo@C NPs/Ag NWs/ PDMS membrane.

Ag NWs coating period from 30 min (Ag30) to 90 min (Ag90) shows the increasing amount of Ag NWs on the surface (Figure S2a, Supporting Information). The surface Ag amount has also been checked by EDS analysis. Figure S2b (Supporting Information) shows that the Ag weight percent on the surface increased from 32% of Ag30 to 96% of Ag90. PDMS dip-coating was implemented after Ag NWs dip-coating, Figure S2c (Supporting Information) reveals that PDMS dip-coating did not change the Ag NWs distribution on the membrane surface. Nevertheless, the Si weight percentage from Figure S2d (Supporting Information) affirms the successful coating of PDMS.

Figure 3a shows the Raman shift of different membranes, 632 cm^{-1} corresponds to the symmetric stretching of the C—C bond in the benzene ring of rPET, peak at 854 cm^{-1} refers to the deformation of the aromatic C—H bonds, 1120 cm^{-1} peak is attributed to the stretching of the C—O bond in the ester group, peak at 1169 cm^{-1} corresponding to C—H stretching peak in the aromatic ring, 1285 cm^{-1} peak stands for the C—C bond stretching in the benzene ring, peak at 1610 cm^{-1} stands for the stretching of carbonyl group, and 1726 cm^{-1} peak corresponds to the acid C═O stretching vibration. The peak at 1280 cm^{-1} from rPET/FeCo@C stands for the D band of the amorphous carbon shell component, and the 1600 cm^{-1} peak corresponds to the G band of the carbon shell of FeCo@C NPs. Figure S3 (Supporting Information) shows the core–shell structure of FeCo@C NPs by TEM images.

Since Ag NWs are synthesized by the polyvinylpyrrolidone (PVP)-assisted polyol method, 1355 cm^{-1} peak from rPET/FeCo@C/Ag90 is attributed to the —CH_2 vibration of PVP and peak at 1567 cm^{-1} corresponding to the C═O stretching of PVP. The 492 cm^{-1} peak of rPET/FeCo@C/Ag90/PDMS20 presents the Si—O—Si stretching of PDMS. Figure S4 (Supporting Information) shows the PVP layer on the surface of Ag NWs by TEM images.

The ATR-FTIR results (Figure 3b) demonstrate that 727 cm^{-1} peak of rPET stands for the C—H bending, 870 and 1014 cm^{-1} peaks present for out-plane and in-plane vibrations of the benzene group respectively, 1092 cm^{-1} corresponds to the C═O stretching of rPET, 1242 cm^{-1} refers to the —CH_2 group, 1414 cm^{-1} peak stands for the aromatic skeletal stretching band, 1720 cm^{-1} corresponds to the C═O stretching and 2960 cm^{-1} peak is attributed to C—H symmetrical stretching of rPET. 806 and 1265 cm^{-1} peaks of rPET/FeCo@C/Ag90/PDMS20 stand for the —CH_3 rocking and symmetric bending in Si–CH_3 bond, 1053 and 1081 cm^{-1} peaks correspond to the Si—O—Si bonds of PDMS, while 2905 and 2983 cm^{-1} peaks stand for the C—H stretching in —CH_3 group of PDMS.

X-ray diffraction (XRD) and X-ray photoelectron spectroscopy (XPS) were used to examine the membrane surface chemistry to prove the existence of inorganic materials. Figure 3c shows no peak of rPET; this is due to the polymer chains consolidated before crystallization during the rapid solvent evaporation of the electrospinning process. The rPET/FeCo@C shows (110), (200), and (211) crystal plane peaks at 44.8°, 65.2°, and 82.6°, which presents the body-centered cubic lattice (BCC) structure of FeCo alloy. The diffract broad peak at 25° presents the amorphous carbon shell structure. The rPET/FeCo@C/Ag90 show five diffraction peaks (111), (200), (220), (311), and (222) at 38.11°, 44.3°, 64.44°, 77.4°, and 81.54° presenting the existence of face-centered cubic (FCC) lattice structure of silver nanostructure. Moreover, the diffraction peaks of rPET/FeCo@C/Ag90/PDMS20 show no changes after PDMS dip-coating.

Figure 3d shows the XPS result of the rPET/FeC0@C/Ag90/PDMS20 membrane and Figure 3g–l shows the binding energies of various elements. Co, Fe, O, Ag, C, and Si could be detected from the rPET/FeCo@C NPs/Ag NWs/PDMS membrane surface. Figure 3g presents the C—C,

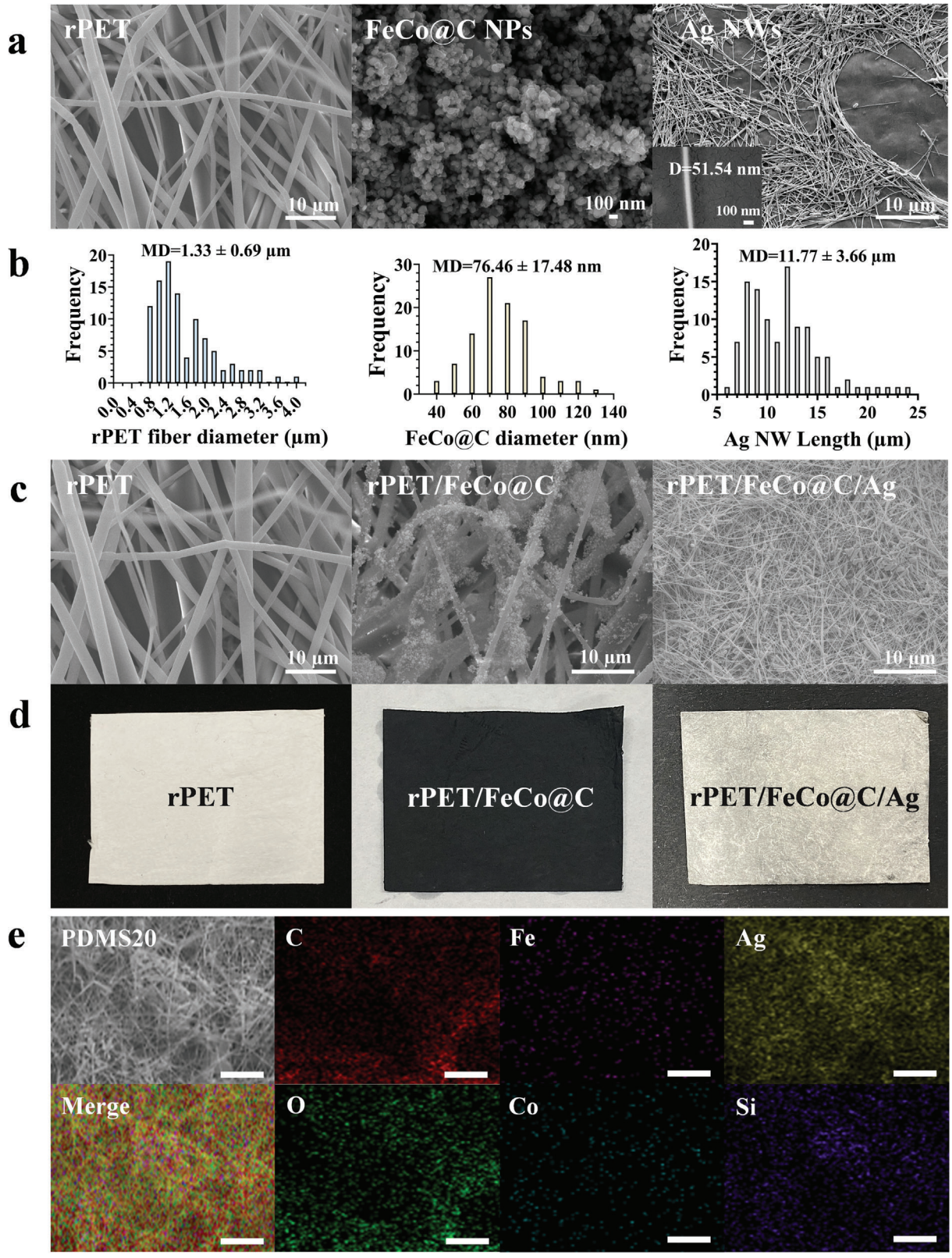

Figure 2. a) The surface morphology and b) the diameter analysis for the rPET electrospun membrane, FeCo@C NPs, and Ag NWs. The surface changes with the subsequent coating of FeCo@C NPs and Ag NWs were evaluated using c) SEM scanning and d) photography. e) The element analysis of the PDMS20 membrane by EDS mapping (scale bar = 5 μm).

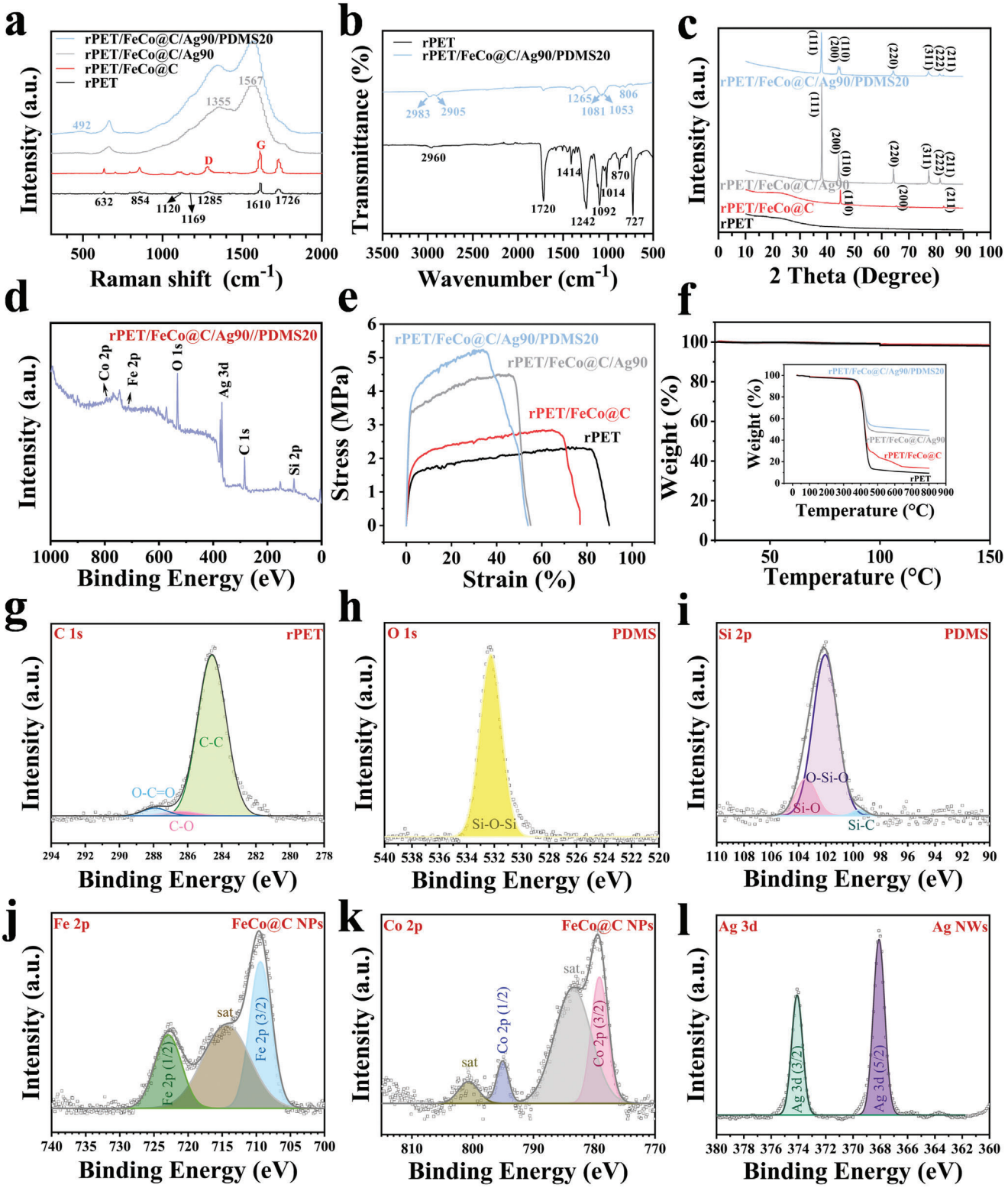

Figure 3. The following analyses were performed on the membranes: a) Raman shift, b) ATR-FTIR, c) XRD, d) XPS, e) tensile test analysis, and f) TGA for rPET, rPET/FeCo@C, rPET/FeCo@C/Ag90, and rPET/FeCo@C/Ag90/PDMS20, respectively. A detailed XPS peak analysis by g) C 1s, h) O 1s, i) Si 2p, j) Fe 2p, k) Co 2p, and l) Ag 3d spectrums.

C—O, and O—C═O bonds at 284.8, 286.6, and 288.4 eV of the C 1s spectrum, which validates the existence of rPET. The Si—O—Si of PDMS could be detected from the O 1s spectrum (Figure 3h) at 532.3 eV, and the Si—C, Si—O, and O—Si—O could be simultaneously found from the Si 2p spectrum (Figure 3i) at 99.6, 102.2 and 103.5 eV respectively. FeCo@C NPs could be verified by the Fe 2p (3/2) and Fe 2p (1/2) at 709.4 and 723 eV of the Fe 2p spectrum (Figure 3j). The 714.6 eV peak from the Fe 2p spectrum stands for the shake-up satellite peak of the Fe component.[43] Figure 3k shows the Co 2p spectrum, Co 2p (3/2), and Co 2p (1/2) of FeCo@C NPs can be detected from 780 and 795.8 eV. The satellite peaks at 784.5 and 800.9 eV of the Co 2p spectrum reveal the oxidized Co component.[43] From Figure 3l, Ag 3d (5/2) and Ag 3d (3/2) of Ag NWs could be detected at 368.2 and 374.1 eV of the Ag 3d spectrum.

Figure 3e shows the tensile test results of membranes. The strain of the rPET substrate is 81.92%, and FeCo@C NPs sonication coating reduced the strain to 69.17%. Ag NWs dip-coating further reduced the strain to 47.42%, and the strain of final rPET/FeCo@C/Ag90/PDMS20 membrane is 35.63%. The membrane strength increased with every processing step from 2.26 MPa of rPET to 5.16 MPa of rPET/FeCo@C/Ag90/PDMS20. Figure 3f shows the thermal stability results of membranes by using thermogravimetric analysis (TGA). The 0.77% loss of weight at 100 °C is due to the membrane moisture evaporation. Despite the moisture elimination, the membrane remains relatively stable under 150 °C. The dramatical weight loss between 400 and 450 °C accounts for the thermal decomposition of the membranes. For the rPET/FeCo@C membrane, the slower weight decreasing between 450 °C and 650 °C is attributed to the reduction of the carbon shell of FeCo@C NPs.

2.2. Joule Heat and Thermotherapy Performances

The excellent electrical conductivity (Figure S5, Supporting Information) of rPET/FeCo@C NPs/Ag NWs/PDMS with extra low voltage provides the potential for safe thermal therapy for rheumatoid arthritis patients and personal thermal management applications. The membrane (3 × 3 cm^2) was connected by a DC power supply, which can offer current to the conductive membrane and generate heat by the collision between the accelerated electrons and phonons.[44] An infrared camera (FLIR E5, USA) was applied to monitor the membrane surface temperature under different voltages. **Figure 4** illustrates how different coating periods of Ag NWs affect the functional relationship between temperature and the square of applied voltages ($R^2 \geq 0.994$). The slopes ascend dramatically from 1.4144 of rPET/FeCo@C/Ag30/PDMS20 to 28.808 of rPET/FeCo@C/Ag90/PDMS20, which demonstrates that the membrane joule heat efficiency improved with the increasing amount of Ag NWs. The rPET/FeCo@C/Ag90/PDMS20 has been selected for the remaining joule heat tests.

The following equation derived from Joule's law is elaborated to explain further the joule heat mechanism of rPET/FeCo@C/Ag90/PDMS20 thermal therapy potential.[45,46]

$$T_s = \left(T_0 + U^2\right) / RhA \quad (1)$$

T_s stands for the saturated temperature of the heating membrane, T_0 stands for the initial temperature before applying voltage on the membrane, U^2, R, h, and A represent the square of external stimuli voltage, the electrical resistance, the convective heat transfer coefficient, and the area of heating membrane respectively. In Figure 4a, the coefficient h is described as R^2, and the temperature will be more reliable, while the value of R^2 tends to be 1.

Figure 4b presents the joule heat details of rPET/FeCo@C/Ag90/PDMS20. The membrane only needs 2 V to reach 137 °C. For the thermal therapy of rheumatoid arthritis patients, it only requires 0.8 V to be applied on the rPET/FeCo@C/Ag90/PDMS20 for heating up to ≈40 °C. The rPET/FeCo@C/Ag90/PDMS20 was monitored under 0.8 V for 1 h to test the membrane heating stability. Figure 4c demonstrates a stable temperature at ≈40 °C, indicating the potential of this membrane for application as a thermal treatment device. Figure 4d verifies that the membrane has an agile electric heating response; the membrane was controlled under 0.4 V increment intervals from 0 to 2 V to carry out the manageable temperature from room temperature to 137 °C. Figure 4e depicts the temperature-changing details of the membrane under 2 V. It took 15 s to reach 100.6 °C and heat up to 138.1 °C at 35 s. The membrane only took 26 s to cool down from 137.4 to 21.5 °C after the current disconnection. Furthermore, the five times repeated switching on/off of the power supply with 0.8 and 2 V, respectively (Figure 4f). The membrane shows a relatively stable temperature, which illustrates the stability for the repeating usage of an electric thermal device. The thermal image results (Figure 4g) illustrate the temperature change of the membrane from 21.8 °C of 0 V to 137 °C of 2 V. Figure S6 (Supporting Information) demonstrates the descending thermal temperature change from 137 °C of 2 V to 21.8 °C of 0 V.

Figure 4h illustrates the joule heat testing circuit, where the DC power supply connects the sample membrane to control the applied voltage. The thermal imager (FLIR E5, USA) monitors the temperature change of the membrane surface. The rPET/FeCo@C/Ag90/PDMS20 membrane exhibits better joule heat performance than most other works, such as copper nanowires (Cu NWs) and carbon nanotubes (CNTs). Meanwhile, comparing the joule heat performance within the temperature range of thermal therapy, this work shows the lowest applied voltage with a safe temperature for thermal therapy application (Figure 4i; Table S1, Supporting Information).

The thermotherapy temperature ranges from 40° to 45° for 15 min to 72 h.[47,48] To examine the thermal therapy device safety for human body joints, the membrane (3 × 3 cm^2) was set on the different joints of the volunteer and heated up to 0.8 V to reach the thermal therapy temperature standard (40–45 °C). The human body test was approved by the Ethical Committee of the SNU IRB (Seoul, Korea) and operated according to the Institutional Review Board of Seoul National University (SNU IRB No.2304/002-004, Korea). **Figure 5a** shows that the voltage increments from 0 to 0.8 V raised the membrane temperature from body temperature to 40.3 °C. It has been asked and recorded that there was no discomfort according to the feedback from the test volunteer. The thermal images also show that only the membrane-targeted area was heated, whereas the uncovered area remained unaffected. It confirms that rPET/FeCo@C/Ag90/PDMS20

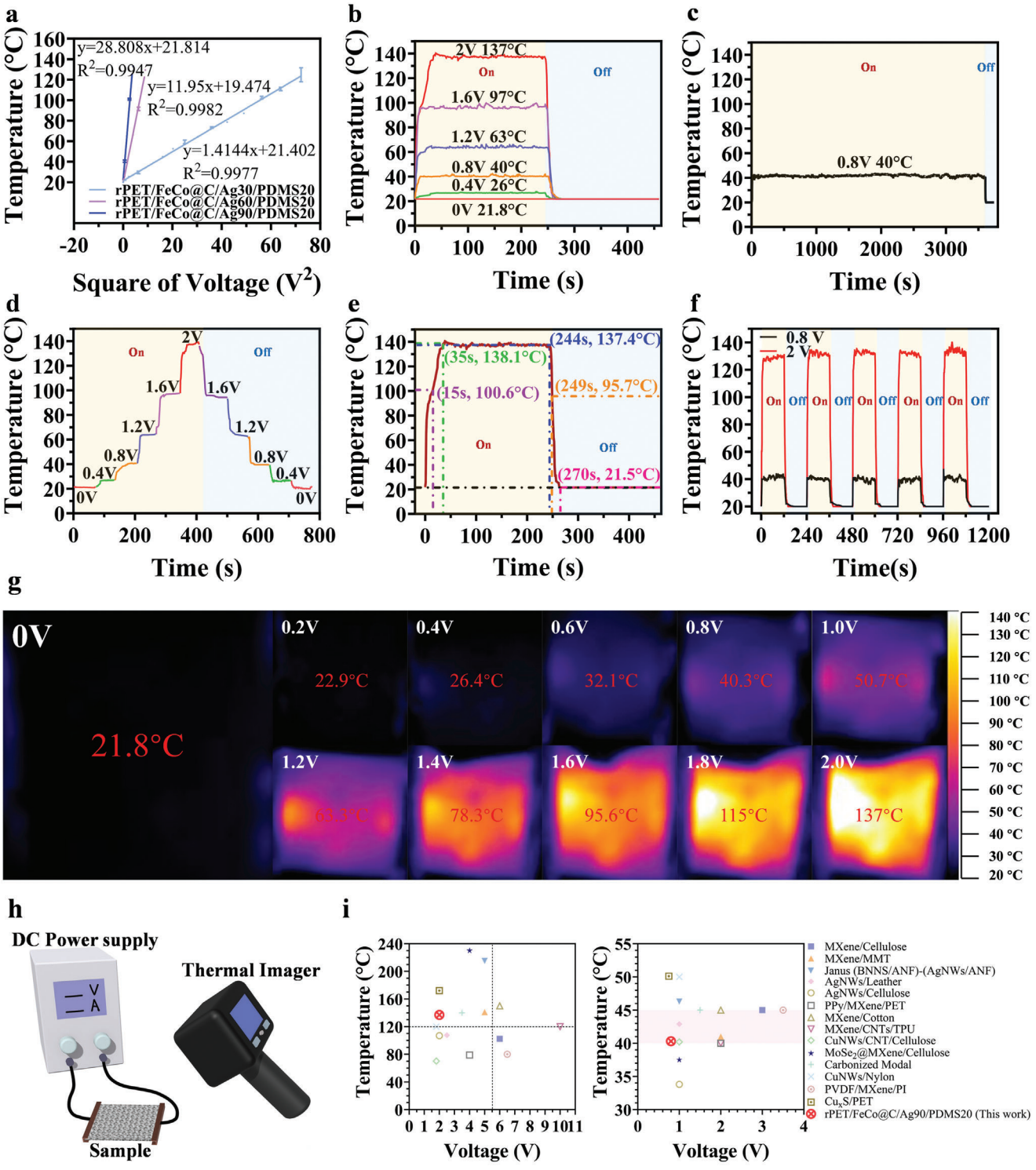

Figure 4. a) The steady values between temperature and the square of voltages for various membranes. (n = 3) The heating behaviors of the rPET/FeCo@C/Ag90/PDMS20 membrane b) under different input voltages, c) the long-term performance at an applied voltage of 0.8 V, d) the on/off behavior with different voltages, e) details analysis of one cycle on/off operation at an applied voltage of 2 V, f) five cycles of on/off operation at applied voltages of 0.8 V and 2 V, respectively. g) The thermal photographs with ascending DC input voltages from 0 V to 2 V. h) The scheme of measuring membrane surface temperature using a thermal imager and a DC power supply. i) The comparison of the membrane maximum temperature and thermal therapy temperature by different voltage supplies with other electrical thermal research studies.

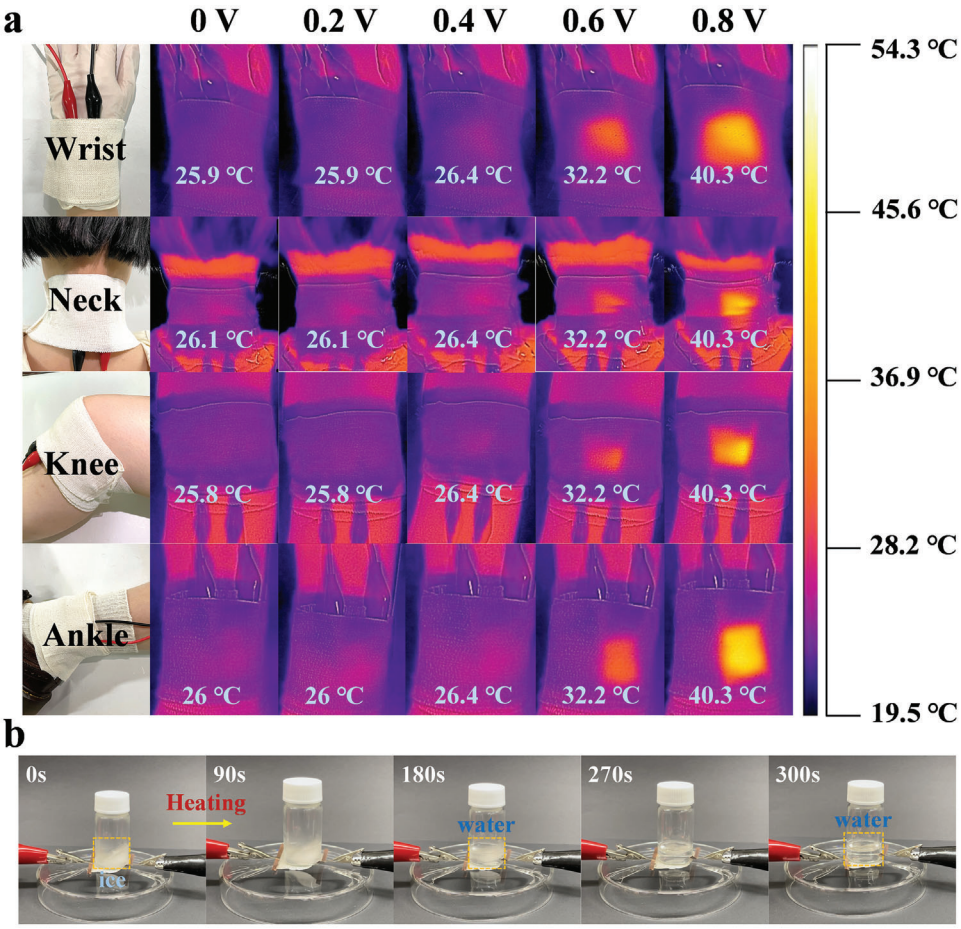

Figure 5. a) The safety assessment of using the rPET/FeCo@C/Ag90/PDMS20 membrane for thermotherapy by heating the membrane to 40.3 °C using an applied voltage ranging from 0 to 0.8 V on the wrist, neck, knee, and ankle, respectively. b) The observation of melting tilting ice (2 mL of DI water) within 300 s under a power supply of 2 V.

has the potential to be applied as a safe thermal therapy device.

Additionally, the rPET/FeCo@C/Ag90/PDMS20 membrane could also be applied to ice melting in extreme environments. The 2 mL DI water was frozen overnight at the tilting angle before the experiment, and Figure 5b shows that the ice could be completely melting under 2 V within 300 s. It can potentially be applied under extreme environments for fast deicing end-use.

2.3. EMI Shielding Performance

Figure 6 shows the EMI shielding results at X-band (8.2–12.4 GHz). The EMI shielding efficiency is usually assessed by the shielding effectiveness in total (SE_T), which is the sum of reflection (SE_R) and absorption (SE_A). The rPET/FeCo@C/Ag90/PDMS20 shows excellent EMI shielding efficiency at ≈68 dB with only 103 µm. Figure 6a indicates the sum effectiveness of absorption (Figure 6b) and reflection (Figure 6c). The observed small fluctuations of Figure 6a–c may be attributed to the free orientation and distribution of conductive network (Ag NWs), which could affect both absorption and reflection loss.[49,50] Figure S7 (Supporting Information) demonstrates a significant enhancement in shielding efficiency for the membrane with FeCo@C NPs compared to the membrane coated solely with pure Ag NWs. Based on the average value of each membrane's absorption, reflection, and total shielding effectiveness in Figure 6d, the shielding effectiveness increased from 27 dB of rPET/Ag30 to 43 dB of rPET/FeCo@C/Ag30, 43 dB of rPET/Ag60 to 61 dB of rPET/FeCo@C/Ag60, 61 dB of rPET/Ag90 to 68 dB of rPET/FeCo@C/Ag90. Thus, the addition of FeCo@C NPs improved the membrane EMI shielding efficiency.

In further exploration of the EMI shielding mechanism, the absorption, reflection, and transmission coefficients are shown in Figure 6e. Based on the reflection coefficient, the increase of Ag NWs coating time improved the reflection of incident waves, and PDMS coating has no measurable effect on the membrane EMI efficiency. The introduction of FeCo@C NPs has improved the membrane's reflection coefficient, and the transmission coefficient of all the membranes is verge to zero, which presents that the membranes have outstanding EMI effects. The EMI SE stability of the developed rPET/FeCo@C/Ag90/PDMS20 membrane has also been tested by comparing the shielding effectiveness and coefficients of the fresh membrane (Figure S8, Supporting

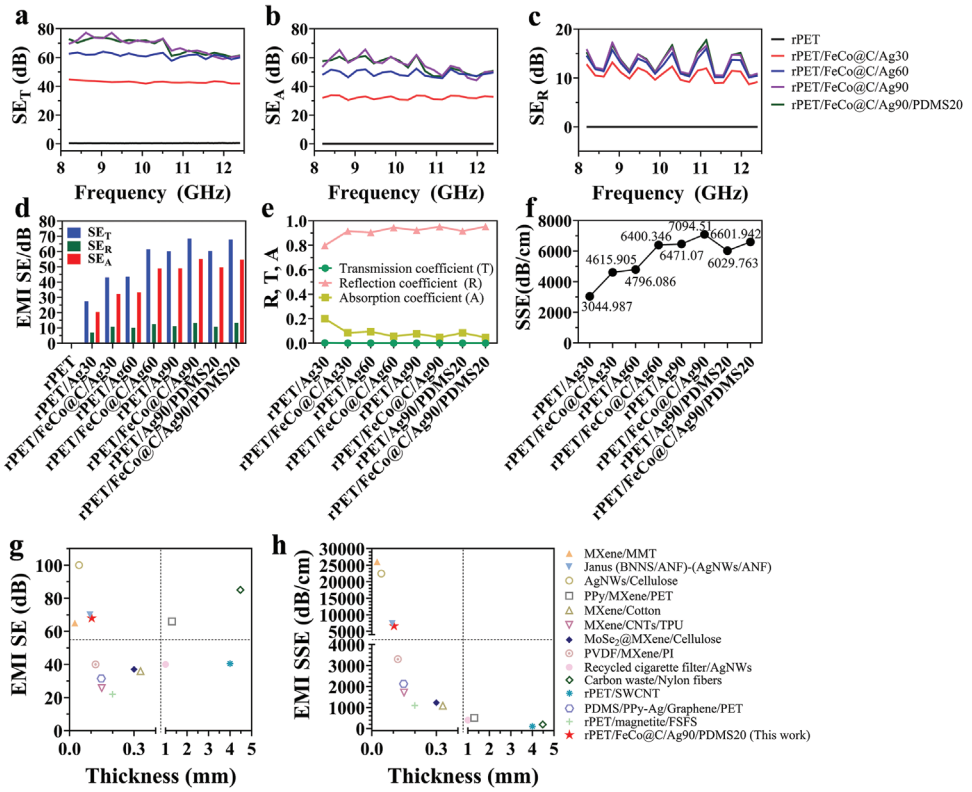

Figure 6. The variation in a) total EMI shielding effectiveness, b) absorption shielding effectiveness, and c) reflection shielding effectiveness of various membranes in the X band. d) The average value calculations of the EMI shielding (total, absorption, reflection) with different membranes. e) Determination of the reflection, absorption, and transmission coefficients of various membranes. f) The EMI SSE of various membranes. The comparison of g) the EMI shielding efficiencies and h) the EMI SSE to membrane thickness with other EMI shielding research studies.

Information). Figure S9 (Supporting Information) also demonstrated the magnetism of flexible rPET/FeCo@C/Ag90/PDMS20 membrane and synthesized FeCo@C NPs by photographs and hysteresis loop test. The FeCo@C NPs show a high saturated magnetization (150.65 emu g^{-1}) and coercivity (138.74 Oe), making it a promising EMI shielding candidate. Figure S10 (Supporting Information) shows the thickness of various developed membranes. Based on the thickness analysis and EMI SE of various developed membranes, Figure 6f delineates the EMI-specific shielding efficiency (EMI SSE) for each membrane. Figure 6g,h compares the developed membrane EMI efficiency with other works. The rPET/FeCo@C/Ag90/PDMS20 membrane tends to be relatively thin (≈0.1 mm) with better EMI shielding efficiency (68 dB) than other works. According to the comparison of EMI SSE, the developed rPET/FeCo@C/Ag90/PDMS20 membrane also shows decent shielding efficiency (≈6602 dB cm^{-1}) with relatively thin thickness among other works (Table S2, Supporting Information).

Figure 7a illustrates the EMI shielding test by a Vector Network Analyzer (N5230A, Agilent Technologies, USA) with an X-band coaxial waveguide adapter to catch the sample between the channels. Figure 7b shows the mechanism of EMI shielding through the rPET/FeCo@C/Ag90/PDMS20 membrane. When the EMI wave contacts the membrane surface, the mismatched impedance between Ag NWs and surrounding air multiple-reflects part of the incident waves (Figure 7c). Ag NWs that possess high conductivity could also improve the interface absorption loss (Figure 7d). The microwaves interact with the high-density electron carriers of accumulated conductive Ag NWs, then get attenuated by the massive ohmic losses and transform into heat energy (Figure 7e). The residue wave then meets the FeCo@C core–shell NPs. The carbon shell reduces the EMI by eddy current loss (Figure 7f), and the magnetic FeCo core resists the microwave propagation by magnetic resonance, magnetic eddy current, domain wall resonance, and hysteresis loss, which leads to magnetic loss (Figure 7f,g).[51] The dipolar polarization between the carbon shell and the FeCo core has also receded the EMI waves (Figure 7h). The remanent transmitted microwaves pass through the EMI shielding membrane afterward.

2.4. Antibacterial Performance

Figure 8a shows that PDMS dip-coating can improve surface hydrophobicity from 0 degrees of Ag90 to 153.9 degrees of PDMS30. The 0 degree of Ag90 is due to the synthesized Ag NWs having a thin hydrophilic PVP coating layer (Figure S4, Supporting Information). The free arrangement of Ag NWs provides a proper surface roughness of the membrane, and the siloxane crosslinking of PDMS on the surface lifts the contact angle.

The inhibition zone test was applied to test the antibacterial properties of the developed membrane. The

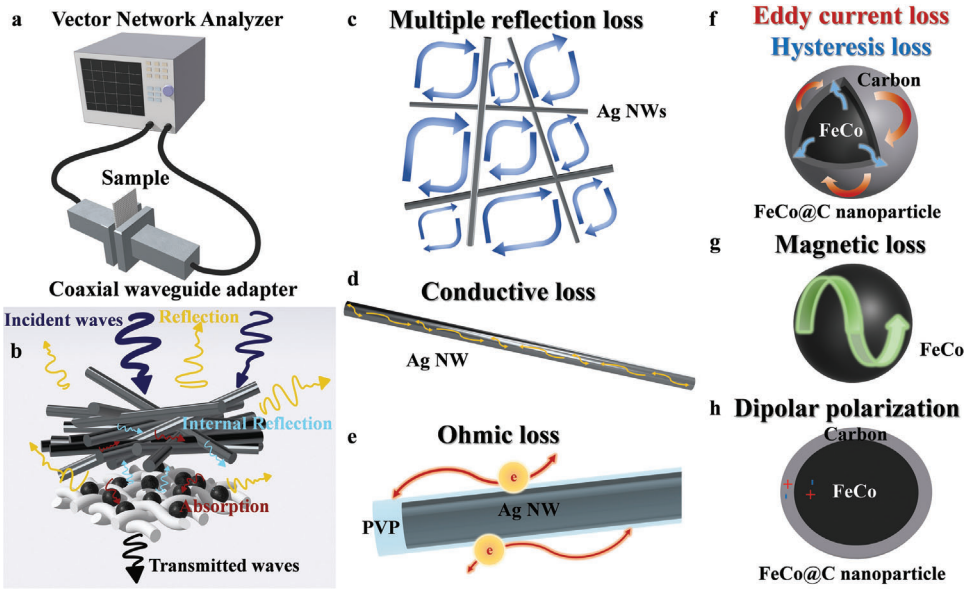

Figure 7. a) The scheme illustration of the EMI shielding efficiency test using a Vector Network Analyzer and a coaxial waveguide adapter. b) The illustration of the membrane EMI shielding principle using the rPET/FeCo@C/Ag90/PDMS20 membrane. c–h) The illustration of EMI dissipation details through the membrane.

inhibition zones of rPET, rPET/FeCo@C, rPET/FeCo@C/Ag90, and rPET/FeCo@C/Ag90/PDMS20 membranes for gram-negative (*Escherichia Coli* DH5*α* and *Pseudomonas aeruginosa*) and gram-positive (*Staphylococcus aureus* and *Bacillus cereus*) bacterium are shown in Figure 8b. The results show that rPET/FeCo@C/Ag90/PDMS20 possesses antibacterial properties against both gram-negative and gram-positive bacteria. Electrospun rPET membrane has no antibacterial capability among all the bacteria. The rPET/FeCo@C membrane shows antibacterial properties against gram-negative *P. aeruginosa* and gram-positive *S. aureus* and *B. cereus* bacterium. FeCo@C NPs possess antibacterial properties by the Fenton reaction of FeCo bimetallic catalysis.[52] It destroys the membrane structure of bacteria and releases the intrinsic H_2O_2, and the synergistic catalysis of Fe and Co ions produces reactive oxygen, which further kills the bacterium.[53]

The rPET/FeCo@C/Ag90 membrane shows an inhibition zone against all four bacteria. The antibacterial property is responsible for the Ag ions release and the synergic action with the bacteria's surface.[54] In addition to inducing the destruction of the bacteria cell membrane, the synergic action of Ag ions could also infiltrate the bacteria and damage the proteins and DNA.[55]

The rPET/FeCo@C/Ag90/PDMS20 membrane generally shows antibacterial capability against all four bacteria. It also presents a slightly bigger inhibition zone comparing

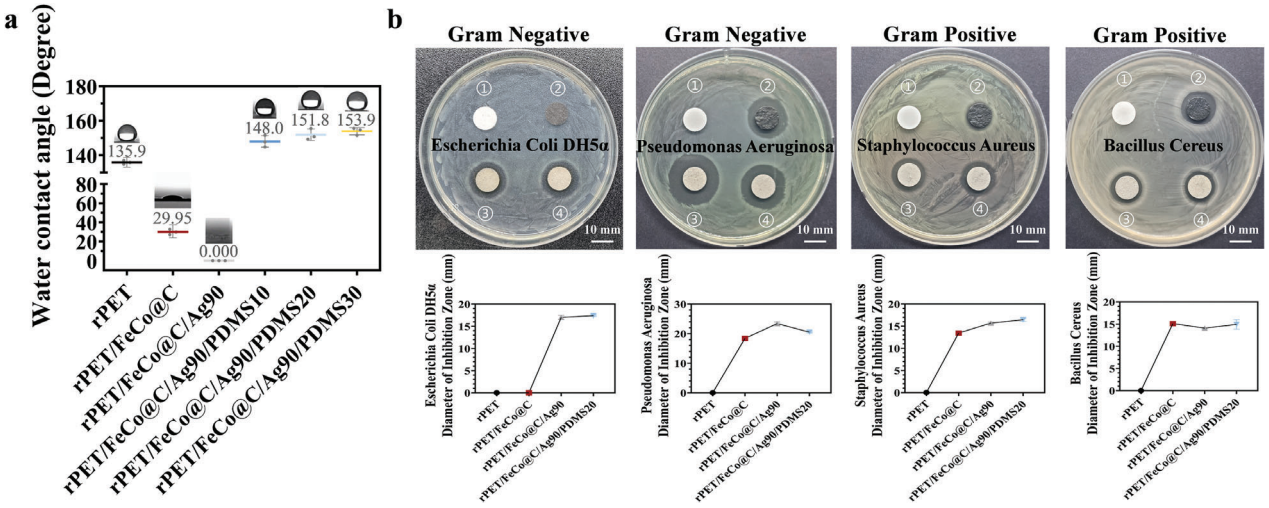

Figure 8. a) The water contact angle of the membrane was measured after each coating ($n = 3$); and b) the inhibition zone of ① rPET, ② rPET/FeCo@C, ③ rPET/FeCo@C/Ag90, ④ rPET/FeCo@C/Ag90/PDMS20 membranes against *E. coli* DH5*α*, *P. aeruginosa*, *S. aureus*, and *B. cereus*. ($n > 5$).

rPET/FeCo@C/Ag90 against *E. coli* DH5α, *S. aureus*, and *B. cereus*. The increasing inhibition zone could account for the membrane surface superhydrophobicity after PDMS coating, which reduces the formation of bacteria clusters by preventing the radial fluid flow of bacteria.[56]

In summary, the developed rPET/FeCo@C/Ag90/PDMS20 membrane possesses antibacterial capabilities, making it a safe and potential candidate for application as a wearable membrane.

3. Conclusion

In this paper, we present a novel EMI shielding membrane with multiple functions, achieved by utilizing an electrospun membrane made from rPET and incorporating magnetic FeCo@C NPs, as well as highly conductive Ag NWs. The membrane was dip-coated with PDMS subsequently to achieve superhydrophobicity and enhanced antibacterial properties against gram-positive and gram-negative bacteria. Remarkably, the membrane exhibits an average shielding efficiency of 68 dB in the X band, with a conductive thickness of only 12.33 µm. Furthermore, it shows excellent and stable electrical conductivity, allowing precise control of joule heat temperature through different power supplies. It reaches 40.3 °C by only 0.8 V for low voltage thermotherapy and attains 137 °C by 2 V for deicing in extreme environments. In conclusion, the multifunctional and sustainable rPET/FeCo@C/Ag90/PDMS20 membrane, characterized by exceptional EMI shielding performance, exhibits significant promise for various applications in next-generation electronics.

4. Experimental Section

Materials: Polyethylene terephthalate (PET) bottles were recycled from JIRISAN Mulhana (FINEBio, Korea). Chloroform (CF) (99.8%), dichloromethane (DCM) (> 99.9%), cobalt (II) nitrate hexahydrate (97%), silver nitrate (99.8%) ethylene glycol (99.5%) and n-hexane (96.0%) were purchased from Samchun pure chemical CO., LTD. Trifluoroacetic acid (TFA) (99%) was purchased from DAEJUNG Chemicals & Metals Co. Polyvinylpyrrolidone (PVP) (Mw = 55000), sodium citrate tribasic dihydrate (99%), and potassium ferricyanide (III) were purchased from Sigma–Aldrich. Sylgard 184 A, B (PDMS prepolymer, curing agent) was purchased from Sewang Hitech Silicone. *E. coli* DH5α was purchased from Invitrogen, *P. aeruginosa* (ATCC 15692), *S. aureus* (ATCC 6538), and *B. cereus* (ATCC 21366) were purchased from the Korean Collection for Type Cultures.

Electrospun rPET Membrane: The recycled plastic bottle was rinsed and cut into 5 × 5 mm^2. The PET cutting pieces were then sanitized twice using 70% ethanol and subjected to sonication for 30 min each time. Subsequently, the PET cutting pieces were dried in a vacuum oven overnight and exposed to UV sterilization for 6 h. The rPET electrospinning solution was prepared by dissolving 2.6 g of PET cutting pieces in a 17.4 g mixture of chloroform, trifluoroacetic acid, and dichloromethane (CF/TFA/DCM) (1:2:7 w/w/w 1.74 g/3.48 g/12.18 g). After thorough dissolution using a magnetic stirrer, the electrospun rPET membrane was fabricated using a voltage of 13 kV, a 23 cm distance between the spinneret and collector drum, and a pumping speed of 1 mL h^{-1} with an 18-gauge needle tip. The membrane was electrospuned for 9 h, followed by pressing with a roller machine (MTI, MSK-MR-100A) for further processing.

Synthesize FeCo@C NPs: In a typical FeCo PBAs synthetic method, solution A was prepared by dissolving 4.0 mmol of $K_3Fe(CN)_6$ in 200 mL of deionized water. In solution B, 6.0 mmol $Co(NO_3)_2{\cdot}6H_2O$ and 9.0 mmol sodium citrate were completely dissolved in another 200 mL of deionized water. Under magnetic stirring, solution A was dropped to solution B. The mixed solution was subsequently aged for 24 h at room temperature. Deionized water and absolute ethanol were used to wash the purple precipitate FeCo PBAs at 8000 rpm centrifugation for 10 min per round until a limpid suspension. The washed solution was vacuum-dried at 60 °C in an oven. The dried FeCo PBAs nanocubes were then pyrolyzed under an argon atmosphere for 2 h in a tube furnace at 600 °C with a heating rate of 2 °C min^{-1}.

Synthesize Ag NWs: Under a magnetic stirrer, the was synthesized by first dissolving 5.2 mmol of polyvinylpyrrolidone in 19 mL of ethylene glycol. 0.6 mL of 0.01 M NaCl in ethylene glycol, 1.6 mL of 0.005 M NaBr in ethylene glycol and 3.5 mmol of $AgNO_3$ in ethylene glycol solutions were added in order with 1 min intervals. The mixed solution was placed and reacted in a preheated 175 °C oil bath with magnetic stirring for 16–18 min. Lastly, the reaction mixture was centrifuged for 5 min at 8000 rpm each time and repeated until a clear supernatant. The Ag NWs were collected and redispersed in ethanol for further use and characterization.

FeCo@C NPs Sonication Coating: The synthesized FeCo@C NPs were dissolved into ethanol with 1 mg mL^{-1}. The electrospun rPET membrane was immersed in 50 mL of FeCo@C NPs/ethanol solution and sonicated for 10 min. The membrane surface turned black after the sonication coating. The sonicated membrane was then dried for the next step.

Ag NWs and PDMS Dip-Coating: The rPET/FeCo@C membrane was immersed into 10 mg mL^{-1} of Ag NWs/ethanol solution for 5 min per time and dried before the next round of dip-coating. The rPET/FeCo@C membrane was coated with different periods (30, 60, 90 min). The dried rPET/FeCo@C/Ag NWs membrane was then dip-coated by 1 wt.% of PDMS/Hexane solution for 10, 20, and 30 min, respectively. The rPET/FeCo@C/Ag NWs/PDMS membrane was dried under a 45 °C vacuum oven overnight and ready for the tests.

Characterizations: The material morphology analysis and the component analysis were performed by SEM (JSM-7800F Prime, Japan). The structure and morphology of FeCo@C core–shell NPs and Ag NWs were observed by TEM (JEM-3010, Japan). The water contact angle of the membrane surface was measured by a contact angle analyzer (Phoenix 300, Korea). Organic materials were characterized by ATR-FTIR TENSOR27 (Bruker, Germany) and Raman DXR2xi (Thermo Fisher Scientific, USA). Inorganic materials were characterized by XRD (D8 discover, Bruker, Germany) and XPS analysis (AXIS-HSi, KRATOS, UK). Membrane thermal stability was tested by the thermogravimetric analysis (TGA/DSC 1, Mettler Toledo) under a nitrogen atmosphere. The mechanical property of the membrane was based on the ASTM standard and measured by the Universal Testing Machine (Instron 5543, USA). The joule heat performance of the membrane was tested by the DC power supply (Wanptek, KPS305DF) and thermal imager (FLIR E5, USA). Membrane thickness was measured by a digital micrometer (MDC-25PX, Mitutoyo, Japan). Membrane resistance was determined by a four-point-probe sheet resistance measurement system (CMT-100s, Advanced Instrument Technology, USA). The hysteresis loop of FeCo@C NPs was measured by VSM (VSM-7410, Lake Shore, USA).

Statistical Analysis: The data within figures and tables were presented as mean value ± standard deviation. All experiments were conducted in triplicate or more, and the specific number of experimental values was indicated in each figure legend. Statistical analyses were carried out using Origin 2020 and one-way ANOVA in Prism (GraphPad, San Diego, CA, USA).

Supporting Information

Supporting Information is available from the Wiley Online Library or from the author.

Acknowledgements

Z.J. and S.P. contributed equally to this work. This work was in part supported by the Research Institute for Convergence Science, Graduate School of Convergence Science and Technology, and Research Institute of

Advanced Materials, Seoul National University. This work was supported by a grant from the Ministry of Trade, Industry, and Energy, Republic of Korea (20018522).

Conflict of Interest

The authors declare no conflict of interest.

Data Availability Statement

The data that support the findings of this study are available on request from the corresponding author. The data are not publicly available due to privacy or ethical restrictions.

Keywords

antibacterial membranes, electromagnetic interference shielding, joule heat, recycled materials, thermal management

Received: December 12, 2023
Revised: January 16, 2024
Published online:

[1] G. Lim, N. Kwon, E. Han, S. Bok, S. Lee, B. Lim, *J. Ind. Eng. Chem.* **2021**, *93*, 245.
[2] Z. Zeng, F. Jiang, Y. Yue, D. Han, L. Lin, S. Zhao, Y.-B. Zhao, Z. Pan, C. Li, G. Nyström, J. Wang, *Adv. Mater.* **2020**, *32*, 1908496.
[3] L. Wang, Z. Ma, Y. Zhang, L. Chen, D. Cao, J. Gu, *SusMat* **2021**, *1*, 413.
[4] C. Liu, L. Wang, S. Liu, L. Tong, X. Liu, *Adv. Ind. Eng. Polym. Res.* **2020**, *3*, 149.
[5] S. Ryu, B. Park, Y. Han, S. Kwon, T. Kim, R. Lamouri, K. Kim, S. Lee, *J. Mater. Chem. A* **2022**, *8*, 4446.
[6] Y. Xie, S. Liu, K. Huang, B. Chen, P. Shi, Z. Chen, B. Liu, K. Liu, Z. Wu, K. Chen, Y. Qi, Z. Liu, *Adv. Mater.* **2022**, *34*, 2202982.
[7] F. Shahzad, M. Alhabeb, C. Hatter, B. Anasori, S. Hong, C. Koo, Y. Gogotsi, *Science* **2016**, *353*, 1137.
[8] Z. Wang, S. Wang, Z. Du, L. Yang, X. Cheng, H. Wang, *Compos. B: Eng.* **2023**, *266*, 110999.
[9] Z. Guo, P. Ren, Z. Wang, J. Tang, F. Zhang, Z. Zong, Z. Chen, Y. Jin, F. Ren, *Compos. B: Eng.* **2022**, *236*, 109836.
[10] C. Li, Y. Han, Q. Du, D. Wu, J. Sun, Z. Wang, L. Zhang, *SusMat* **2023**, *3*, 345.
[11] T. Tran, D. Vo, S. Nguyen, C. Vu, *Compos. Part A Appl. Sci. Manuf.* **2021**, *149*, 106485.
[12] K. Wang, C. Chen, Q. Zheng, J. Xiong, H. Liu, L. Yang, Y. Chen, H. Li, *Carbon* **2022**, *197*, 87.
[13] E. Pakdel, S. Kashi, T. Baum, K. Usman, J. Razal, R. Varley, X. Wang, *J. Clean. Prod.* **2021**, *315*, 128196.
[14] T. Zhang, S. Zeng, H. Jiang, Z. Li, D. Bai, Y. Li, J. Li, *ACS Appl. Mater. Interfaces* **2021**, *13*, 11332.
[15] C. Lee, C. Lin, L. Wang, Y. Lee, *Chem. Eng. J.* **2023**, *468*, 143447.
[16] M. Tas, U. Musa, I. Ahmed, F. Xu, C. Smartt, X. Hou, *Polym* **2022**, *240*, 124499.
[17] C. Li, L. Tong, S. Wang, Q. Liu, Y. Wang, X. Li, M. Wang, M. Li, X. Chen, J. Wu, Q. Chen, Y. Mai, W. Fan, Y. Chen, X. Li, *SusMat* **2023**, *3*, 431.
[18] F. Ding, S. Zhang, X. Chen, R. Li, X. Ren, *Compos. B: Eng.* **2022**, *235*, 109791.
[19] S. Park, S. Kim, *Fash. Text.* **2014**, *1*, 1.
[20] B. Sadeghi, Y. Marfavi, R. AliAkbari, E. Kowsari, F. Ajdari, S. Ramakrishna, *Mater. Circ. Econ.* **2021**, *3*, 4.
[21] J. Song, Q. Zhao, C. Meng, J. Meng, J. Chen, J. Li, *ACS Appl. Mater. Interfaces* **2021**, *13*, 49380.
[22] A. You, X. Zhang, X. Peng, K. Dong, Y. Lu, Q. Zhang, *Macromol. Mater. Eng.* **2021**, *306*, 2100147.
[23] M. Nasr, A. Shubbar, Z. Abed, M. Ibrahim, *J. Build. Eng.* **2020**, *31*, 101444.
[24] J. Jhang, T. Lin, T. Lin, Y. Chen, C. Lou, J. Lin, *Polym. Compos.* **2020**, *41*, 2768.
[25] A. Majumdar, S. Shukla, A. Singh, S. Arora, *Resour. Conserv. Recycl.* **2020**, *161*, 104915.
[26] M. Dulal, S. Afroj, J. Ahn, Y. Cho, C. Carr, I. Kim, N. Karim, *ACS Nano* **2022**, *16*, 19755.
[27] A. Baggio, H. Doan, P. Vo, K. Kinashi, W. Sakai, N. Tsutsumi, Y. Fuse, M. Sangermano, *Global Chall.* **2021**, *5*, 2000107.
[28] Y. Chen, B. Zhao, H. Zhang, T. Zhang, D. Yang, F. Qiu, *Chem. Eng. J.* **2022**, *450*, 138177.
[29] J. Xu, R. Li, S. Ji, B. Zhao, T. Cui, X. Tan, G. Gou, J. Jian, H. Xu, Y. Qiao, Y. Yang, S. Zhang, T. Ren, *ACS Nano* **2021**, *15*, 8907.
[30] Y. Chen, Z. Wang, R. Xu, W. Wang, D. Yu, *Chem. Eng. J.* **2020**, *394*, 124960.
[31] J. Wu, M. Wang, L. Dong, J. Shi, M. Ohyama, Y. Kohsaka, C. Zhu, H. Morikawa, *ACS Nano* **2022**, *16*, 12801.
[32] Y. Zhang, K. Ruan, J. Gu, *Small* **2021**, *17*, 2101951.
[33] D. Kuang, L. Hou, S. Wang, H. Luo, L. Deng, J. Mead, H. Huang, M. Song, *Carbon* **2019**, *153*, 52.
[34] D. Li, B. Zhang, W. Liu, X. Liang, G. Ji, *Dalton Trans.* **2017**, *43*, 14926.
[35] W. Zeng, L. Shu, Q. Li, S. Chen, F. Wang, X. Tao, *Adv. Mater.* **2014**, *26*, 5310.
[36] J. Heo, J. Eom, Y. Kim, S. Park, *Small* **2018**, *14*, 1703034.
[37] F. Zhang, J. Hu, P. Zhao, P. He, H. Mi, Z. Guo, C. Liu, C. Shen, *Compos. Part A Appl. Sci. Manuf.* **2021**, *147*, 106472.
[38] Z. Ma, S. Kang, J. Ma, L. Shao, A. Wei, C. Liang, J. Gu, B. Yang, D. Dong, L. Wei, Z. Ji, *ACS Nano* **2019**, *13*, 7578.
[39] J. Gao, W. Li, H. Shi, M. Hu, R. Li, *Compos. Sci. Technol.* **2014**, *92*, 95.
[40] D. Pu, W. Zhou, Y. Li, J. Chen, J. Chen, H. Zhang, B. Mi, L. Wang, Y. Ma, *RSC Adv.* **2015**, *122*, 100725.
[41] J. Huang, R. Fan, S. Connor, P. Yang, *Angew. Chem., Int. Ed.* **2007**, *46*, 2414.
[42] E. Jang, T. Kang, H. Im, D. Kim, Y. Kim, *Small* **2008**, *4*, 2255.
[43] K. Yu, P. Shi, J. Fan, Y. Min, Q. Xu, *J. Nanoparticle Res.* **2019**, *21*, 230.
[44] Y. Cui, Z. Jiang, G. Zheng, W. Wang, M. Zhou, P. Wang, Y. Yu, Q. Wang, *Chem. Eng. J.* **2022**, *446*, 137189.
[45] J. Xie, Y. Zhang, J. Dai, Z. Xie, J. Xue, K. Dai, F. Zhang, D. Liu, J. Cheng, F. Kang, B. Li, Y. Zhao, L. Lin, Q. Zheng, *Small* **2023**, *19*, 2205853.
[46] Z. Ma, S. Kang, J. Ma, L. Shao, Y. Zhang, C. Liu, A. Wei, X. Xiang, L. Wei, J. Gu, *ACS Nano* **2020**, *14*, 8368.
[47] R. Habash, R. Bansal, D. Krewski, H. Alhafid, *Crit Rev Biomed Eng* **2006**, *34*, 459.
[48] L. Lepak, *Physical Rehabilitation*, W.B. Saunders, Philadelphia, PA, USA, **2007**, p 117.
[49] E. Mikinka, M. Siwak, *J. Mater. Sci. Mater. Electron.* **2021**, *32*, 24585.
[50] B. U. Durmaz, A. O. Salman, A. Aytac, *ACS Omega* **2023**, *8*, 22762.
[51] J. Chang, H. Zhai, Z. Hu, J. Li, *Compos. B Eng.* **2022**, *246*, 110269.
[52] X. Meng, F. Zhang, H. Guo, C. Zhang, H. Hu, W. Wang, J. Liu, X. Shuai, Z. Cao, *Adv. Healthcare Mater.* **2021**, *10*, 2100780.
[53] F. Kuang, Y. Chen, W. Shan, Y. Li, X. Bao, X. Gao, D. An, M. Qiu, *J. Mater. Chem. B* **2022**, *29*, 5582.
[54] M. Polívková, V. Štrublová, T. Hubáček, S. Rimpelová, V. Švorčík, J. Siegel, *Mater. Sci. Eng. C* **2017**, *72*, 512.
[55] X. Xie, C. Mao, X. Liu, Y. Zhang, Z. Cui, X. Yang, K. Yeung, H. Pan, P. Chu, S. Wu, *ACS Appl. Mater. Interfaces* **2017**, *9*, 26417.
[56] J. Seyfi, V. Goodarzi, F. Wurm, S. Shojaei, M. Jafari-Nodoushan, N. Najmoddin, H. Khonakdar, M. Baghersad, L. Uzun, *Prog. Org. Coat.* **2020**, *149*, 105944.